nature geoscience

Article

https://doi.org/10.1038/s41561-023-01297-x

Millennial atmospheric CO_2 changes linked to ocean ventilation modes over past 150,000 years

In the format provided by the authors and unedited

Supplementary Information

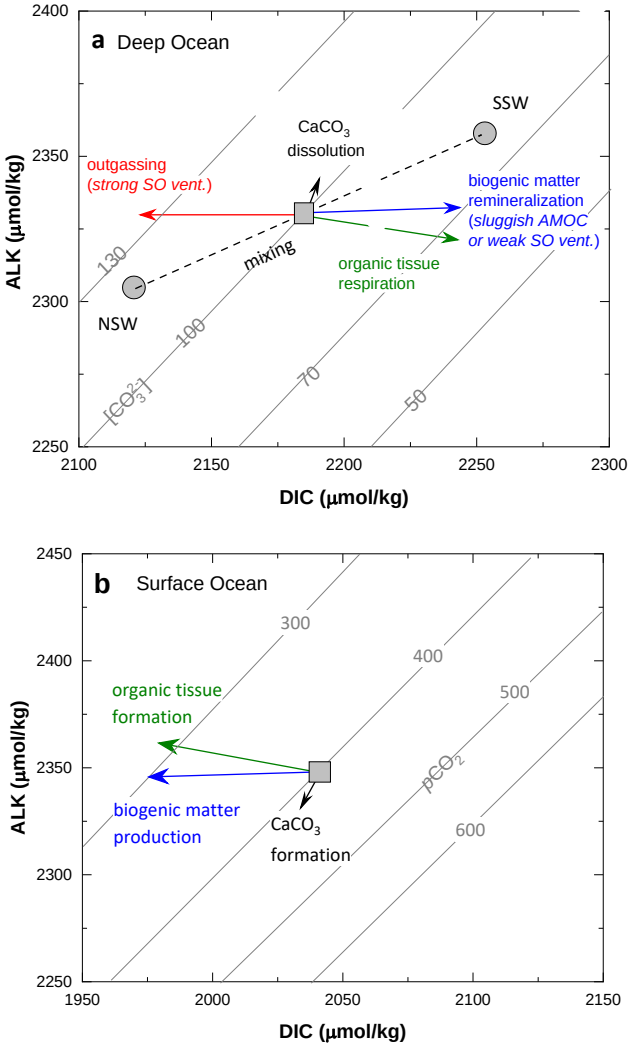

Supplementary Fig. 1 | Processes affecting deep-water [CO_3^{2-}] and atmospheric CO_2. a, Deep ocean ALK-DIC-[CO_3^{2-}]. **b**, Surface ocean ALK-DIC-pCO_2. ALK: alkalinity; DIC: dissolved inorganic carbon; pCO_2: partial pressure of CO_2; NSW: northern-sourced waters; SSW: southern-sourced waters; SO: Southern Ocean. For CO_2 system calculations[1], we use temperature = 3°C, pressure = 2500 dbar, and S = 35‰ in **a,** and temperature = 25°C, pressure = 5 dbar, and S = 35‰ in **b**. Preindustrial SSW and NSW endmember values are shown by circles, and their mixing is indicated by the dashed line (**a**). For illustration purpose, square represents ~1:1 NSW-SSW mixing. Enhanced Southern Ocean ventilation would decrease DIC and increase [CO_3^{2-}] in the deep ocean (red arrow; **a**). Reduced ventilation in the Southern Ocean and/or North Atlantic (sluggish AMOC) would promote accumulation of products of biogenic matter respiration in the ocean interior, decreasing deep-water [CO_3^{2-}] (blue arrow; **a**). This is likely accompanied by an increased ocean biological pump efficiency which would lower pCO_2 in the surface ocean and thereby the atmosphere (blue arrow; **b**). Note that biological processes include cycling of both "soft" organic tissues (green arrows) and "hard-part" $CaCO_3$ (black arrows), but "soft" tissue recycling dominantly affects seawater [CO_3^{2-}] and pCO_2[2-5]. Biogenic matter cycling generally causes opposite changes in seawater [CO_3^{2-}] and DIC. As can be seen, seawater [CO_3^{2-}] can place constraints on deep ocean ventilation and air-sea carbon exchange.

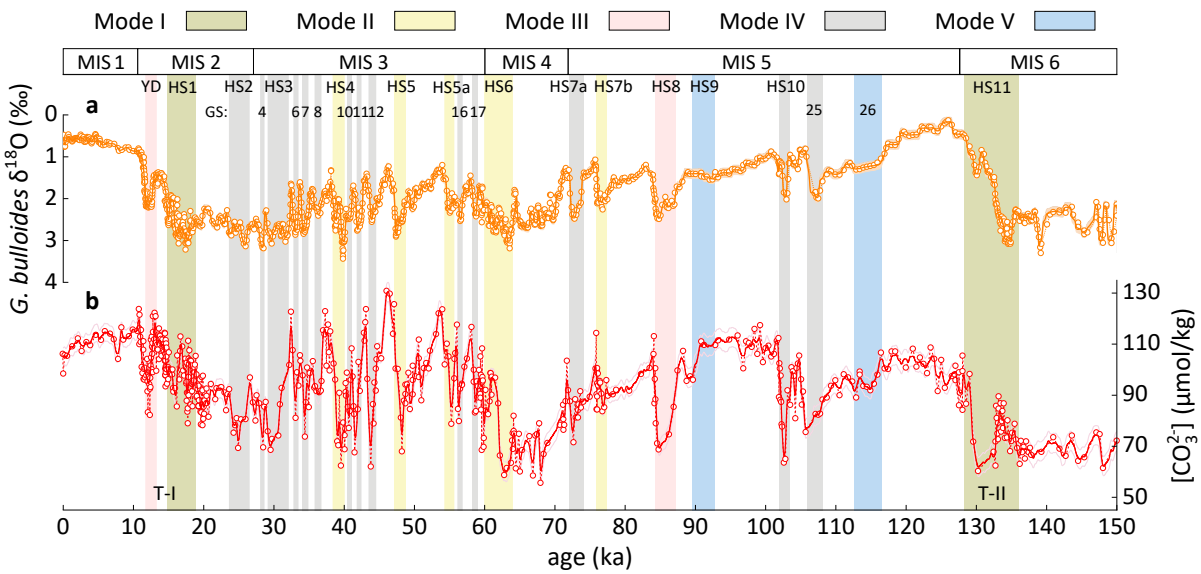

Supplementary Fig. 2 | Monte Carlo-style probabilistic assessments of *G. bulloides* $\delta^{18}O$ and deep-water $[CO_3^{2-}]$ at MD95-2039. a, *G. bulloides* $\delta^{18}O$ (ref. [6] and this study). **b,** Deep-water $[CO_3^{2-}]$ (this study). Bold curves show probability maxima with shading envelopes representing 2σ uncertainty. Vertical bandings with different colours denote the five ventilation modes discussed in the main text.

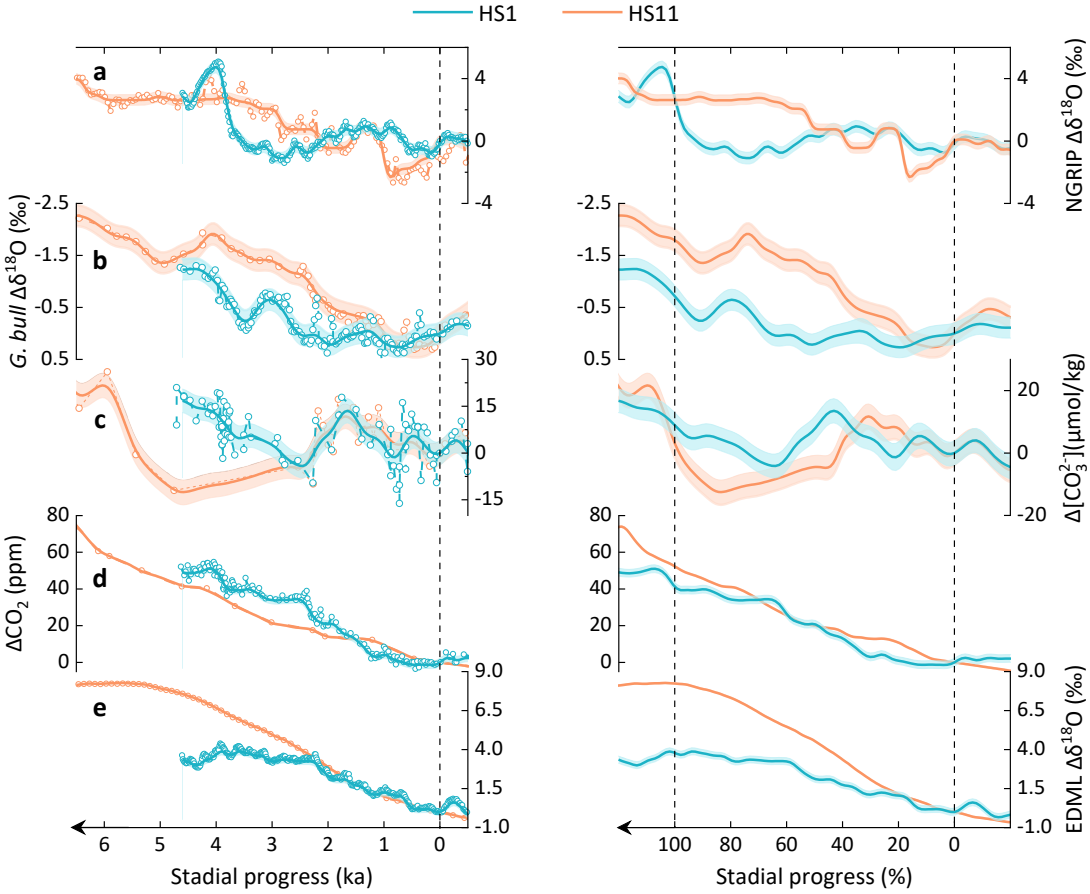

Supplementary Fig. 3 | Mode I stadials. a, NGRIP ice-core $\delta^{18}O$[7]. **b,** MD95-2039 *G. bulloides* $\delta^{18}O$[6, this study]. **c,** Deep-water $[CO_3^{2-}]$ at MD95-2039 (this study). **d,** Ice-core CO_2[8-11]. **e,** EDML $\delta^{18}O$[12]. Changes in parameters shown represent anomalies (Δ) relative to the onset of each stadial. The left panels show anomalies against the elapse time in ka relative to the onset of each stadial. To facilitate comparison, we have normalized the age to 0-100% (right panels). The dash lines indicate the onset (0%) and end (100%) of stadials. In **a**, ODP976 data[13] are used for HS11. Bold curves show probability maxima with shading envelopes representing 2σ uncertainty. See Methods for calculation details.

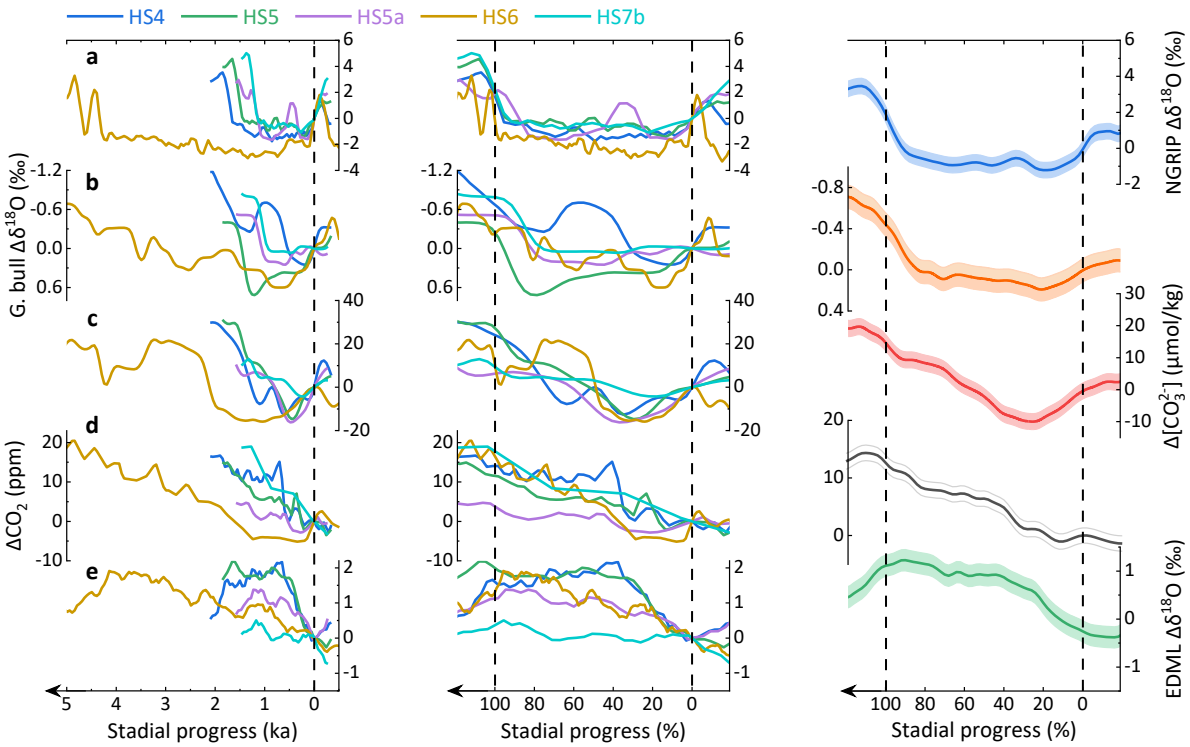

Supplementary Fig. 4 | Mode II stadials. Left and middle panels as Supplementary Fig. 3, but for mode II stadials. The right column shows "stacked" changes of all mode II stadials. Bold curves show probability maxima with shading envelopes representing 2σ uncertainty. For clarity, error envelopes are not shown in left and middle columns.

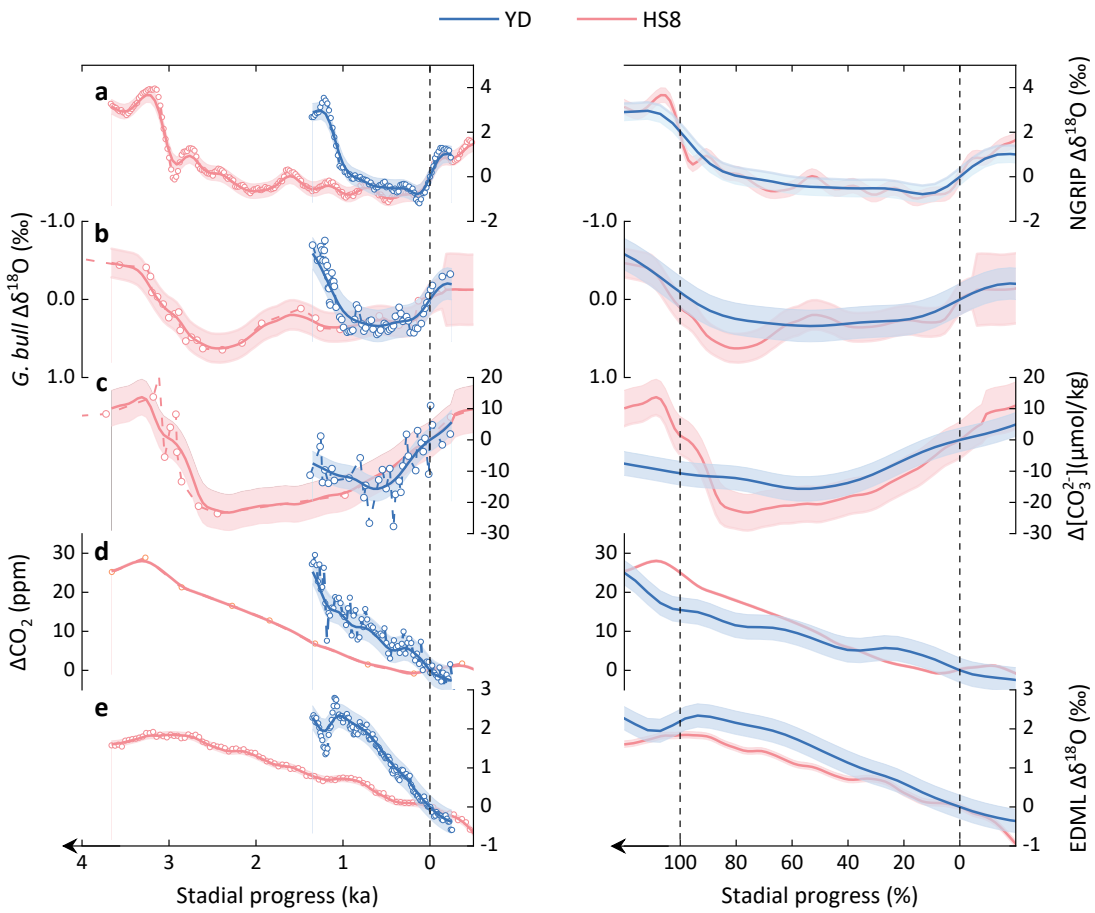

Supplementary Fig. 5 | Mode III stadials. As Supplementary Fig. 3, but for mode III stadials. Bold curves show probability maxima with shading envelopes representing 2σ uncertainty.

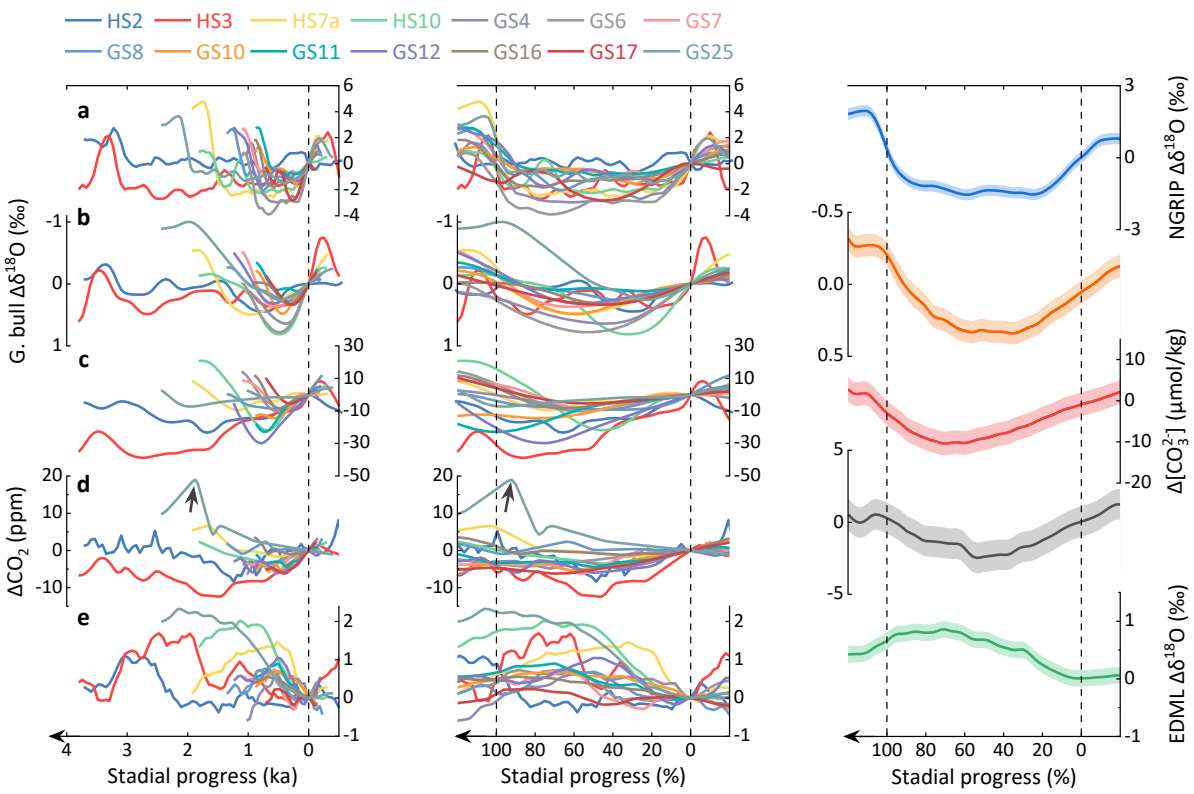

Supplementary Fig. 6 | Mode IV stadials. As Supplementary Fig. 3, but for mode IV stadials. Note that atmospheric CO_2 rise during the late GS25 is driven by a single anomalously high data point (indicated by arrows) whose reliability warrants checking in the future. Bold curves show probability maxima with shading envelopes representing 2σ uncertainty. For clarity, error envelopes are not shown in left and middle columns.

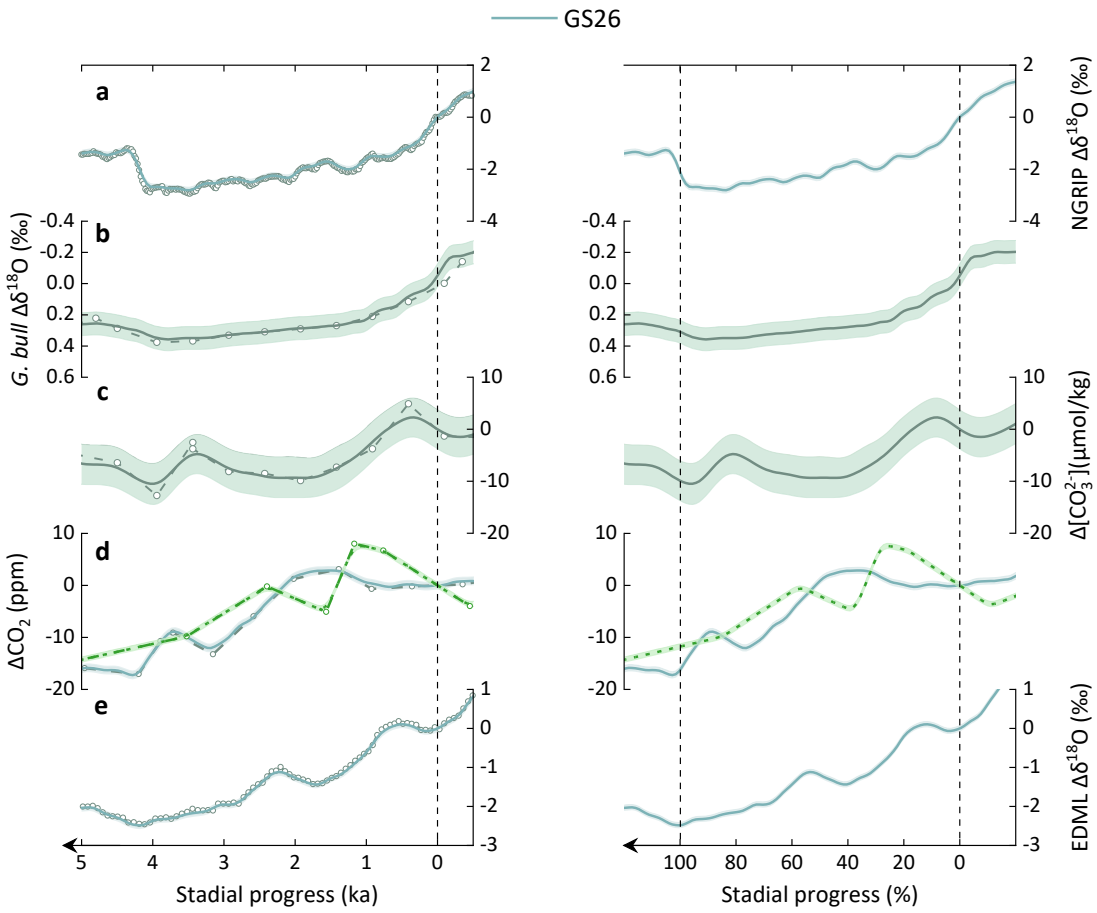

Supplementary Fig. 7 | Mode V stadial. As Supplementary Fig. 3, but for mode V stadial. In **d**, the atmospheric CO_2 record from the Vostok ice core[14] (dashed green; placed on the AICC2012 age model) is also shown to highlight possible age uncertainties at around GS26. Compared to the EDC atmospheric CO_2 record, the timing of the Vostok CO_2 decline was closer to that of deep-water $[CO_3^{2-}]$ at MD95-2039. Here, we treat the atmospheric CO_2 decline to be coeval with the $[CO_3^{2-}]$ decline observed in core MD95-2039 at the last glacial inception. Bold curves show probability maxima with shading envelopes representing 2σ uncertainty.

Supplementary Table 1. Radiocarbon dates for MD95-2039.

mid cm	S-ANU#	$F^{14}C$	±1σ	^{14}C age yr	±1σ yr	lower yr	upper yr	median yr	±1σ yr
79	55406	0.2975	0.0011	9738	34	10318	10652	10495	167
95	55407	0.2862	0.0011	10049	36	10775	11110	10936	167.5
103	55409	0.2748	0.0011	10375	37	11214	11553	11396	169.5
145	55413	0.2276	0.0010	11891	40	13086	13334	13215	124
153	55414	0.2137	0.0010	12398	41	13613	13935	13779	161
161	55416	0.2058	0.0009	12698	41	14002	14419	14214	208.5

Measurements were made using 4-6 mg *G. bulloides* (300-355 μm) from 2 cm sediment depth intervals. Radiocarbon dates are converted into calendar ages using Calib8.1 with ΔR = 0 ± 100 years and the Marine20 curve[15,16].

Supplementary Table 2. Age model tie points for MD95-2039.

Mid cm	age ka	sed rate cm/ka	age control method	age model type
1	0.00		assumed	assumed
79	10.50	7.43	14C	14C
95	10.94	36.28	14C	14C
103	11.40	17.39	14C	14C
115	11.65	47.24	*G. bull* δ^{18}O-NGRIP	AICC2012
142	12.80	23.48	*G. bull* δ^{18}O-NGRIP	AICC2012
145	13.22	7.23	14C	14C
153	13.78	14.18	14C	14C
161	14.21	18.39	14C	14C
175	14.60	36.27	*G. bull* δ^{18}O-NGRIP	AICC2012
240	16.00	46.43	*G. bull* δ^{18}O to Hulu speleothem	Hulu U/Th age
306	17.70	38.82	*G. bull* δ^{18}O to Hulu speleothem	Hulu U/Th age
512	23.55	35.23	*G. bull* δ^{18}O-NGRIP	WDC2014
680	27.98	37.94	*G. bull* δ^{18}O-NGRIP	WDC2014
720	29.08	36.14	*G. bull* δ^{18}O-NGRIP	WDC2014
840	32.70	33.12	*G. bull* δ^{18}O-NGRIP	WDC2014
875	33.91	28.98	*G. bull* δ^{18}O-NGRIP	WDC2014
932	35.69	32.00	*G. bull* δ^{18}O-NGRIP	WDC2014
985	38.44	19.29	*G. bull* δ^{18}O-NGRIP	WDC2014
1045	40.12	35.73	*G. bull* δ^{18}O-NGRIP	WDC2014
1052	40.28	43.75	*G. bull* δ^{18}O-NGRIP	WDC2014
1095	41.75	29.25	*G. bull* δ^{18}O-NGRIP	WDC2014
1133	43.58	20.73	*G. bull* δ^{18}O-NGRIP	WDC2014
1157	44.81	19.55	*G. bull* δ^{18}O-NGRIP	WDC2014
1187	47.10	13.08	*G. bull* δ^{18}O-NGRIP	WDC2014
1230	48.60	28.68	*G. bull* δ^{18}O-NGRIP	WDC2014
1239	49.58	9.22	*G. bull* δ^{18}O-NGRIP	WDC2014
1295	54.49	11.40	*G. bull* δ^{18}O-NGRIP	WDC2014
1321	55.98	17.46	*G. bull* δ^{18}O-NGRIP	WDC2014
1367.5	59.37	13.71	*G. bull* δ^{18}O-NGRIP	WDC2014
1386.5	59.70	57.22	*G. bull* δ^{18}O-NGRIP	WDC2014
1459.25	64.13	16.43	*G. bull* δ^{18}O-NGRIP	WDC2014
1468.5	64.25	76.60	*G. bull* δ^{18}O-NGRIP	WDC2014
1538.5	69.43	13.52	*G. bull* δ^{18}O-NGRIP	AICC2012
1568.5	72.15	11.03	*G. bull* δ^{18}O-NGRIP	AICC2012
1578	73.70	6.13	*G. bull* δ^{18}O-NGRIP	AICC2012
1590	75.75	5.85	*G. bull* δ^{18}O-NGRIP	AICC2012
1602	76.03	42.86	*G. bull* δ^{18}O-NGRIP	AICC2012
1612	76.80	12.99	*G. bull* δ^{18}O-NGRIP	AICC2012

Supplementary Table 2. continued.

Mid cm	age ka	sed rate cm/ka	age control method	age model type
1622.5	78.40	6.56	*G. bull* δ^{18}O-NGRIP	AICC2012
1658.5	83.95	6.49	*G. bull* δ^{18}O-NGRIP	AICC2012
1678.5	84.60	30.77	*G. bull* δ^{18}O-NGRIP	AICC2012
1702	87.25	8.87	*G. bull* δ^{18}O-NGRIP	AICC2012
1775	101.80	5.02	*G. bull* δ^{18}O-NGRIP	AICC2012
1794	102.40	31.67	*G. bull* δ^{18}O-NGRIP	AICC2012
1802	103.22	9.76	*G. bull* δ^{18}O-NGRIP	AICC2012
1829	105.70	10.89	*G. bull* δ^{18}O-NGRIP	AICC2012
1846.5	107.95	7.78	*G. bull* δ^{18}O-NGRIP	AICC2012
1862	112.64	3.30	*G. bull* δ^{18}O-NGRIP	AICC2012
1927	129.04	3.96	δ^{18}O to ODP 976	U-Th/AICC2012
1947	132.45	5.87	δ^{18}O to ODP 976	U-Th/AICC2012
1981	133.98	22.22	δ^{18}O to ODP 976	U-Th/AICC2012
2005	135.08	21.82	δ^{18}O to ODP 976	U-Th/AICC2012
2052	139.36	10.98	δ^{18}O to ODP 976	U-Th/AICC2012
2125	145.81	11.32	*G. bull* δ^{18}O- GL_T_syn	AICC2012
2130	147.09	3.91	*G. bull* δ^{18}O- GL_T_syn	AICC2012
2160	148.51	21.13	*G. bull* δ^{18}O- GL_T_syn	AICC2012
2185	150.35	13.59	*G. bull* δ^{18}O- GL_T_syn	AICC2012

References

1 Pelletier, G., Lewis, E. & Wallace, D. *A calculator for the CO_2 system in seawater for Microsoft Excel/VBA*. 1.0 edn, (Washington State Department of Ecology, Olympia, WA, 2005).

2 Zeebe, R. E. & Wolf-Gladrow, D. A. *CO_2 in Seawater: Equilibrium, Kinetics, Isotopes*. Vol. 65 (Elsevier, 2001).

3 Yu, J. M., Elderfield, H. & Piotrowski, A. Seawater carbonate ion-δ^{13}C systematics and application to glacial-interglacial North Atlantic ocean circulation. *Earth Planet. Sci. Lett.* **271**, 209-220. doi:210.1016/j.epsl.2008.1004.1010 (2008).

4 Yu, J. *et al.* More efficient North Atlantic carbon pump during the Last Glacial Maximum. *Nat Commun* **10**, https://doi.org/10.1038/s41467-41019-10028-z, doi:ARTN 2170, 10.1038/s41467-019-10028-z (2019).

5 Yu, J. *et al.* Sequestration of carbon in the deep Atlantic during the last glaciation. *Nature Geoscience* **9**, 319-324, doi:10.1038/NGEO2657 (2016).

6 Schonfeld, J., Zahn, R. & de Abreu, L. Surface and deep water response to rapid climate changes at the Western Iberian Margin. *Global and Planetary Change* **36**, 237-264, doi:10.1016/S0921-8181(02)00197-2 (2003).

7 NGRIP_members. High-resolution record of Northern Hemisphere climate extending into the last interglacial period. *Nature* **431**, 147-151, doi:Doi 10.1038/Nature02805 (2004).

8 Bereiter, B. *et al.* Revision of the EPICA Dome C CO2 record from 800 to 600 kyr before present. *Geophysical Research Letters* **42**, 542-549, doi:10.1002/2014gl061957 (2015).
9 Ahn, J. & Brook, E. J. Siple Dome ice reveals two modes of millennial CO2 change during the last ice age. *Nat Commun* **5**, doi:Doi 10.1038/Ncomms4723 (2014).
10 Bauska, T. K., Marcott, S. A. & Brook, E. J. Abrupt changes in the global carbon cycle during the last glacial period. *Nature Geoscience* **14**, 91-96, doi:10.1038/s41561-020-00680-2 (2021).
11 Bereiter, B. *et al.* Mode change of millennial CO2 variability during the last glacial cycle associated with a bipolar marine carbon seesaw. *P Natl Acad Sci USA* **109**, 9755-9760, doi:DOI 10.1073/pnas.1204069109 (2012).
12 Barbante, C. *et al.* One-to-one coupling of glacial climate variability in Greenland and Antarctica. *Nature* **444**, 195-198, doi:10.1038/nature05301 (2006).
13 Marino, G. *et al.* Bipolar seesaw control on last interglacial sea level. *Nature* **522**, 197, doi:10.1038/nature14499 (2015).
14 Lüthi, D. *et al.* High-resolution carbon dioxide concentration record 650,000–800,000 years before present. *Nature* **453**, 379-382, doi:doi:10.1038/nature06949 (2008).
15 Heaton, T. J. *et al.* Marine20—The Marine Radiocarbon Age Calibration Curve (0–55,000 cal BP). *Radiocarbon* **62**, 779-820, doi:10.1017/RDC.2020.68 (2020).
16 Stuiver, M. & Reimer, P. J. CALIB rev. 8. *Radiocarbon* **35**, 215-230 (1993).